Acta Oceanol. Sin., 2017, Vol. 36, No. 8, P. 76–83
DOI: 10.1007/s13131-017-1022-2
http://www.hyxb.org.cn
E-mail: hyxbe@263.net

Sea ice extent retrieval with HY-2A scatterometer data and its assessment

SHI Lijian[1, 2*], LI Mingming[3], ZHAO Chaofang[3, 5], WANG Zhixiong[3], SHI Yingni[3, 4], ZOU Juhong[1, 2], ZENG Tao[1, 2]

[1] National Satellite Ocean Application Service, Beijing 100081, China

[2] Key Laboratory of Space Ocean Remote Sensing and Application, State Oceanic Administration, Beijing 100081, China

[3] College of Information Science and Engineering, Ocean University of China, Qingdao 266100, China

[4] Unit 61741 of PLA, Beijing 100094, China

[5] Laboratory for Regional Oceanography and Numerical Modeling, Qingdao National Laboratory for Marine Science and Technology, Qingdao 266100, China

Received 23 May 2016; accepted 4 July 2016

Abstract

A sea ice extent retrieval algorithm over the polar area based on scatterometer data of HY-2A satellite has been established. Four parameters are used for distinguishing between sea ice and ocean with Fisher's linear discriminant analysis method. The method is used to generate polar sea ice extent maps of the Arctic and Antarctic regions of the full 2013–2014 from the scatterometer aboard HY-2A (HY-2A-SCAT) backscatter data. The time series of the ice mapped imagery shows ice edge evolution and indicates a similar seasonal change trend with total ice area from DMSP-F17 Special Sensor Microwave Imager/Sounder (SSMIS) sea ice concentration data. For both hemispheres, the HY-2A-SCAT extent correlates very well with SSMIS 15% extent for the whole year period. Compared with Synthetic Aperture Radar (SAR) imagery, the HY-2A-SCAT ice extent shows good correlation with the Sentinel-1 SAR ice edge. Over some ice edge area, the difference is very evident because sea ice edges can be very dynamic and move several kilometers in a single day.

Key words: Antarctica, Arctic, sea ice extent, HY-2A, scatterometer

Citation: Shi Lijian, Li Mingming, Zhao Chaofang, Wang Zhixiong, Shi Yingni, Zou Juhong, Zeng Tao. 2017. Sea ice extent retrieval with HY-2A scatterometer data and its assessment. Acta Oceanologica Sinica, 36(8): 76–83, doi: 10.1007/s13131-017-1022-2

1 Introduction

Sea ice plays a key role in the earth's climate system and its observation by satellite remote sensing sensors is an important task in climate research. Additionally, sea ice information is important in securing navigation and other offshore activities. Sea ice extent is one parameter used to describe the sea ice condition and microwave sensors are crucial tools because of their independence from sunlight and atmospheric influences.

Two types of microwave sensors are used to detect sea ice extent: passive microwave radiometers, which observe the natural emissions from the ice surface, and active microwave scatterometers, which collect the energy reflected from the ice surface. Since the 1990s, C band Ku band microwave scatterometers, such as NSCAT (NASA Scatterometer), QuikSCAT (Quick Scatterometer) and ASCAT (Advanced Scatterometer), is used for detecting sea ice over the polar area (Long and Drinkwater, 1994; Yueh et al., 1997). The Remund/Long-NSCAT (RL-N) algorithm was demonstrated to map sea ice from Ku-band NSCAT data based on reconstructed backscatter images (Remund and Long, 1997). An adaptation of the RL sea ice extent algorithm for SeaWinds incorporates an iterative maximum likelihood discrimination method to statistically segment the sea ice and ocean (Remund and Long, 2014). The accuracy of the RL-N method could be considerably affected by strong sea surface winds and the melt of summer ice (De Abreu et al., 2002). The Royal Netherlands Meteorological Institute (KNMI) developed a sea ice detection method for ERS, ASCAT and SeaWinds (De Haan and Stoffelen, 2001; Breivik et al., 2012), where computed residuals of the geophysical ice and ocean model functions are interpreted as probabilities and then combined with prior information on the sea ice state using a Bayesian discrimination algorithm to produce sea ice maps. The main difference between the RL and KNMI sea ice detection algorithms is that the former ice and ocean cluster centroids in the four-dimensional space of $\{\sigma^0_{\rm H}, \sigma^0_{\rm V}/\sigma^0_{\rm H}, \Delta\sigma^0_{\rm H,V}\}$ combinations are replaced by actual geophysical model functions for ocean and ice in the original space of SeaWinds backs-

Foundation item: The National Key Research and Development Program of China under contract Nos 2016YFC1402704 and 2016YFC1401007; the Open Research Fund of Key Laboratory of Digital Earth Science, Institute of Remote Sensing and Digital Earth, Chinese Academy of Sciences under contract No. 2014LDE009; the International Science and Technology Cooperation Project of China under contract No. 2011DFA22260; the National Natural Science Foundation of China under contract Nos U1606405 and 41276181; the Chinese Polar Environment Comprehensive Investigation & Assessment Program by the State Oceanic Administration under contract Nos 2015-02-04 and 2015-04-03-02.

*Corresponding author, E-mail: shilj@mail.nsoas.org.cn

catter quadruplets $\{(\sigma^0_{\rm H},\sigma^0_{\rm H})_{\rm fore},(\sigma^0_{\rm H},\sigma^0_{\rm H})_{\rm aft}\}$ (Rivas and Stoffelen, 2011). In addition, a sea surface temperature filter is added in the KNMI algorithm to weaken errors caused by occasional erratic winds over sea ice surfaces. De Abreu et al. (2002) showed that the retrieved ice edge successfully maps heavy areas of pack ice with ice concentrations above 70%, but it detects neither thin ice below 15-cm thickness nor areas of low ice concentration. Other algorithms that combine the active polarization ratio of QuikScat L2B products and the SSM/I 19-GHz passive polarization ratio have also been developed to detect new ice (Tonboe and Toudal, 2005).

HY-2A is the first Chinese satellite designed to monitor the dynamic marine environment. The purpose of this paper is to develop the sea ice extent over the polar area based on the scatterometer data of HY-2A. In the following two sections, details of the data and methods used are introduced. Assessments using other satellite data and other sea ice product are described in Section 4, and conclusions are drawn in Section 5.

2 Dataset

2.1 *HY-2A scatterometer data*

On August 16, 2011, the "HY-2A" satellite was launched in China. It is equipped with four remote microwave sensors: radar altimeter, microwave scatterometer, scanning microwave radiometer and calibration microwave radiometer. The satellite orbits the Earth at a flight height of 973 km and has an inclination angle of 99.34° and an orbit period of 104.46 min. The scatterometer aboard HY-2A satellite (hereafter referred to as HY-2A-SCAT) employs a rotating pencil beam antenna which transmits and receives at 13.256 GHz. Observations of the backscatter cross section (σ^0) are collected in a horizontally polarized (HH) inner beam and vertically polarized (VV) outer beam at incidence angles of 41° and 48°, respectively. The H-polarization covers a swath of 1 350 km and for V-polarization is 1 700 km. HY-2A-SCAT shares a similar sun-synchronous near polar with orbital inclinations of 99.34° at 971 km, and runs an every-day 13+11/14 circle. Hence, the coverage patterns of the sensors are enough that σ^0 measurements of HY-2A-SCAT can be used for detecting polar sea ice.

To study polar sea ice, the National Snow and Ice Data Center (NSIDC) specified a projection plane or grid tangent to Earth's surface at 70 degrees northern and southern latitude with little or no distortion in the marginal ice zone. The 25 km resolution grid dimensions were defined by 448×304 and 332×316 in the Arctic and Antarctic, respectively. The HY-2A-SCAT daily 13+11/14 track σ^0 measurements are reconstructed to a polar plane grid using polar stereographic projection formulae with a resolution of 25 km, which is the same as the previous transform. Of course, each pixel on the polar grid contains either multiple different azimuth and incidence σ^0 measurements or none. Figure 1 exhibits the HY-2A-SCAT ability of observing the polar zone, because the Antarctic continent restricts sea ice from extending beyond about 75° south latitude, and the Arctic sea ice extend all the way to the North Pole.

The HY-2A-SCAT σ^0 measurement data from 2013–2014 were used in this study and 30 days' data of HY-2A-SCAT are missing because of the sensor's instability. The data of 2013 were used to find the ice-ocean discrimination rule of Fisher's linear discriminant analysis (FLDA) method. Then all 2013–2014 data were used to calculate the ice extent. Other data for October and November 2015 were used for sea ice extent visual comparison with Synthetic Aperture Radar (SAR) images.

2.2 *Sea ice concentration from NSIDC*

NSIDC supplies sea ice concentrations (SIC) for both the Northern and Southern Hemispheres with NASA Team algorithm and brightness temperature data derived from the following sensors: the Nimbus-7 Scanning Multichannel Microwave Radiometer, the Defense Meteorological Satellite Program (DMSP), -F8, -F11, and -F13 Special Sensor Microwave/Imagers (SSM/Is), and the DMSP-F17 Special Sensor Microwave Imager/Sounder (SSMIS). The data are provided in a polar stereographic projection at a grid cell size of 25 km×25 km (Parkinson et al., 1996). SIC data from 2013 were used find the ice-ocean discrimination rule of FLDA method. SIC data for 2013–2014 were used to calculate the sea ice extent and to compare with the results of HY-2A-SCAT.

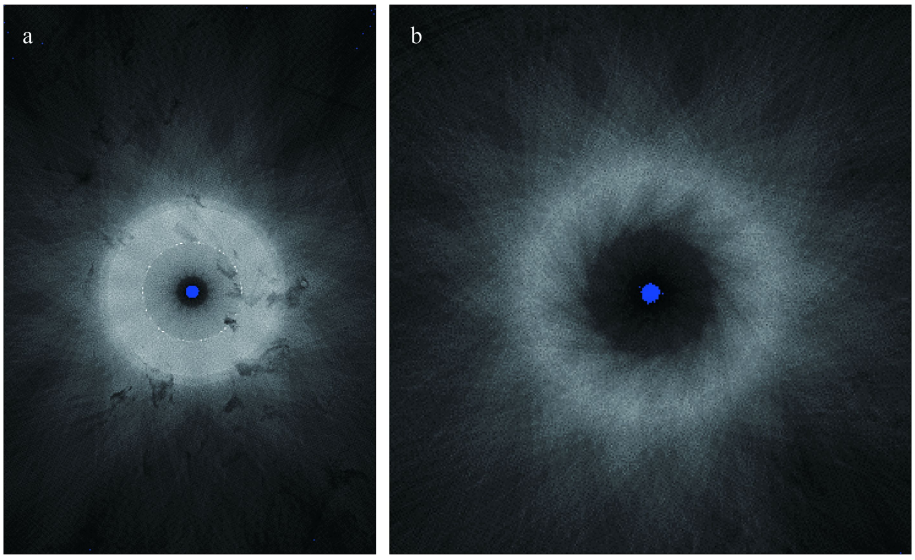

Fig. 1. Reconstructed HY- 2A-SCAT σ^0 distribution in the Arctic (a) and Antarctic (b) on September 20, 2013. The average daily north and south images have 0–40 σ^0 per pixel and major concentrations in 5–25 and 3–15 observations, respectively. The blue is no observation and the other represents effective observation.

2.3 *SAR imagery*

With high spatial resolution, SAR imagery is used for ice edge validation in small localized regions in this study (Remund and Long, 2014). A number of Sentinel-1A images were obtained from the Polar View. The Polar View, an international consortium providing a wide variety of earth observation products that monitor the polar regions and mid-latitude areas affected by ice and snow, provides a near-real-time sea ice information service for ship operators. Full resolution SAR imageries of Sentinel-1 and Radarsat-2 of the past 30 days are supplied free and daily from the Polar View's website with gray scale, Geotiff format and Polar Stereographic projection. Sentinel-1A images, with a 40 m pixel spacing and observed under Extra Wide (EW) swath mode, were selected for qualitative visual validation.

3 Method

Combining the FLDA method with image erosion and dilation techniques, sea ice extent is effectively mapped using four parameters of HY-2A scatterometer measurements. Figure 2 show the flowchart of the algorithm and each step is described in the following sub-sections.

3.1 *Parameter calculation*

In this study, four parameters are used for distinguishing between sea ice and ocean: mean HH backscatter (σ_H) per pixel with an incidence angle of 41°; backscatter polarization ratio (σ_V/σ_H) per pixel for VV and HH; daily standard deviation per pixel for HH ($\Delta\sigma_H$); and daily standard deviation per pixel for VV ($\Delta\sigma_V$). Mean VV backscatter (σ_V) per pixel at an incidence angle of 48° is not used because it has the same trend as σ_H. Figure 3 shows these parameter images and the land mask are provided from NSIDC. Unfortunately, the VV or HH σ^0 measurements per pixel in the daily images are not likely to exist because there is no observation of therm resulting in σ_V/σ_H and $\Delta\sigma_{H,V}$ being unavailable for coincident pixels. Therefore less than two HH and VV measurements are regarded as bad pixels not discriminating sea ice. To remedy this situation, we use the measurements from the previous day to replace the bad pixels.

In generally, the polarization ratio (σ_V/σ_H) reacts to the backscatter difference of polarization and the incidence angle relies on ocean and sea ice. In other words, because sea ice is more strongly isotropic in incidence angle than ocean surfaces (Early and Long, 1997), the polarization ratio (in decibels) is low in sea ice portions of the image and relatively higher in ocean areas (Remund and Long, 2014). Regrettably, high wind induces roughness on ocean surface, thus some ocean packs exhibit low polarization ratios close to those of sea ice (Remund and Long, 1999). In order to overcome this, the horizontally polarized mean measurements (σ_H) and daily standard deviation $\Delta\sigma_{H,V}$ are combined for ice-ocean classification. The h-pol mean measurements were chosen instead of the v-pol, because they have much lower backscatter over the ocean and the sea ice has similar signatures. Meanwhile, the daily standard deviation ($\Delta\sigma_{H,V}$) carries a backscatter response that depends on azimuthal and temporal data,

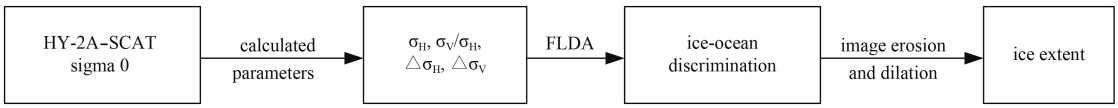

Fig. 2. Flowchart of algorithm.

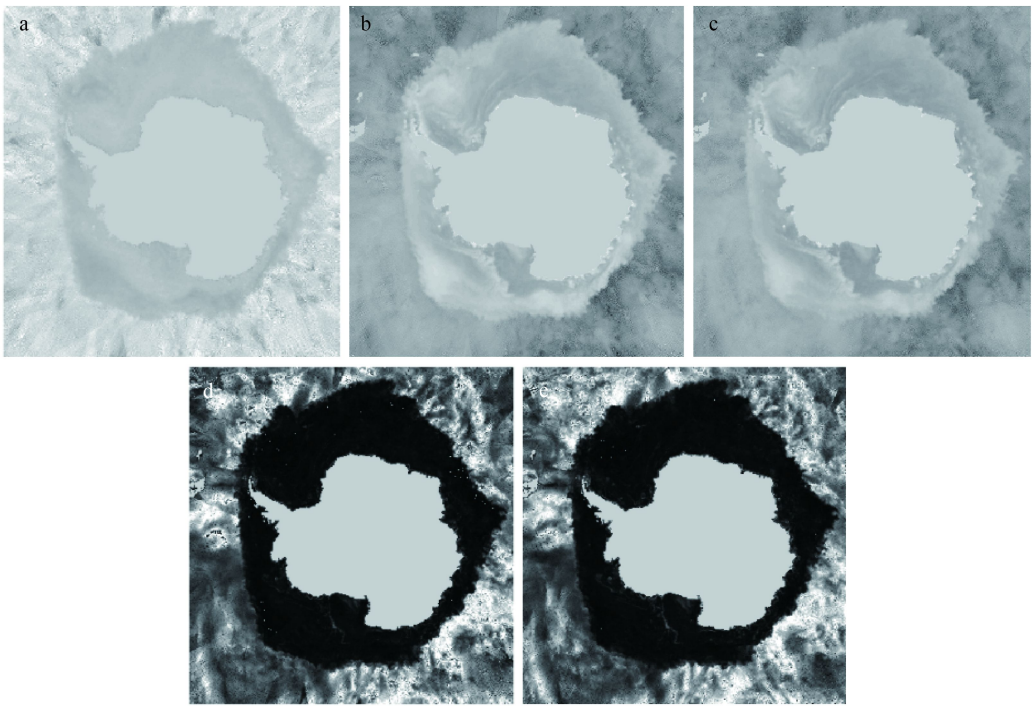

Fig. 3. Five parameter images for σ_V/σ_H (a), σ_H (b), σ_V (c), $\Delta\sigma_H$ (d) and $\Delta\sigma_V$ (e) on September 20, 2013. They contain 332×316 piexls with a space dimension of 25 km in the Antarctic (Arctic images are not shown). Lighter greys without the central continent indicate larger polarization distinctions (a), higher σ^0 reception (b and d), and higher σ^0 variability (c and e).

and sea ice backscatter signatures have demonstrated that the azimuthal dependences are lower than the ocean dependences (Early and Long, 1997; Remund et al., 1997).

3.2 *Ice-ocean discrimination*

The ice-ocean discrimination is achieved through FLDA. This arithmetic fully utilizes the four priori feature parameters of ice-ocean and, by assuming multivariate normal distributions for the two classes, finds the optimal projection vector derived from Fisher's criterion peak for maximum infra-class margin and minimum inter-class cohesion in a new small dimensional space. That is, the data belonging to the same category would be located near each other and the data belonging to the different categories would be far apart. Of course, the FLDA is a supervised linear feature extraction classification method, and the four parameters from HY-2A-SCAT and SIC provided by NSIDC of 2013 were used as the training dataset to search an optimal projection vector. In the training dataset, the area of SIC above 0% was set as sea ice and the other area of SIC equal to 0% was set as ocean.

Assuming that n samples with d dimensions are classified to two classes, and named $x_1, \ldots, x_n \in R^d$, n_1 in front of the sample belongs to class ω_1, n_2 belongs to class ω_2, and both obey the Gaussian distribution with a covariance matrix. Each kind of sample mean μ_i (i=1, 2) and the overall sample mean are

$$\mu_i = \frac{1}{n_i}\sum_{x\in\omega_i} x, \quad i = 1, 2, \tag{1}$$

$$\mu = \frac{1}{n}\sum_{i=1}^{n} x_i. \tag{2}$$

The infra-class dispersion matrix $\boldsymbol{S}_\mathrm{b}$ and the inter-class dispersion matrix $\boldsymbol{S}_\mathrm{w}$ can be expressed as below:

$$\boldsymbol{S}_\mathrm{b} = \sum_{i=1}^{\omega} p(i)\,(\mu_i - \mu)\,(\mu_i - \mu)^\mathrm{T}, p(i) = \frac{n_i}{n}, \tag{3}$$

$$\boldsymbol{S}_\mathrm{w} = \sum_{i=1}^{\omega} \frac{p(i)}{n_i}\sum_{x\in\omega_i} (x - \mu_i)\,(x - \mu_i)^\mathrm{T}, i = 1, 2. \tag{4}$$

Namely, the infra-class variance is more important than the inter-class variance in the discrimination. Then, Fisher's criterion is introduced to seek a hyperplane φ to maximize $(\frac{\varphi^\mathrm{T}\boldsymbol{S}_\mathrm{b}\varphi}{\varphi^\mathrm{T}\boldsymbol{S}_\mathrm{w}\varphi})$ and optimally separate the two classes, and φ is explicitly given in the form:

$$\varphi = \boldsymbol{S}_\mathrm{w}^{-1}\boldsymbol{S}_\mathrm{b}. \tag{5}$$

The optimal projection vector is obtained by solving a general eigenvalue problem as the eigenvector corresponding to the largest eigenvalue of the matrix $\boldsymbol{S}_\mathrm{w}^{-1}\boldsymbol{S}_\mathrm{b}$. Then the four parameters were projected to a one dimensional linear space and the distribution center of the sea ice and open water in the one dimensional space were calculated.

With the above optimal projection vector and distribution center, the parameters of each unclassified pixel were projected and the distances to the distribution center of the sea ice and ocean are computed, and then pixel is classified to the class with the relatively shorter distance. Figure 4a shows the sea ice extent result of FLDA. While the ice edge can be observed apparently, errors still exist. Therefore, residual error filtering is required to improve the ice mapping.

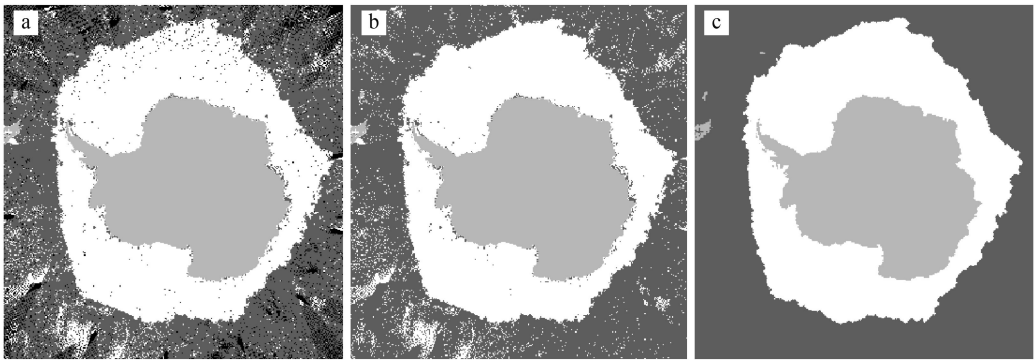

Fig. 4. These grayscate maps of Antartic sea ice on September 20, 2013 through these steps: a. FLDA discrimination with the affection of no observations or invalid parameters (black portion), b. no observation elimination depending on the preivous day's categories, and c. misclassification reduction by binary image processing methods.

3.3 *Misclassification reduction*

Because there are no observations and parameter controls, the parameters of some pixels in the daily polar gird images cannot discriminate between sea ice and ocean. For processing the operational HY-2A-SCAT daily sea ice extent, the NASA Team sea ice extent (archived by NSIDC) is initially a priori information to complement the unclassified pixels whether sea ice or ocean, and used to map the first intact HY2A-SCAT sea ice extent in the polar region. Later the previous day's sea ice extents from HY-2A-SCAT are regarded as a background field for independently producing the real-time sea ice extent maps, such as shown in Fig. 4b.

However, high persistent winds over the ocean can cause ocean pixels to be misclassified as ice (left bottom part of Fig. 4b), and other physical mechanisms may also cause sea ice to be misclassified as ocean. These misclassifications occur in patches or isolated pixels during the imaging period, and the former is much more common than the latter. Polar sea water connectedness helps eliminate the misclassified ocean in the ice by using image erosion and dilation techniques (Remund et al., 2000). This adopts a diamond structure element of radius 2 to implement primary image erosion for eliminating small particle ocean noise and smoothing right ocean edge, and second image dilation for

recovering ocean areas. Next, the misclassified ice in the ocean is a certain distance from the main ice, relative to the previous day's maximum ice edge, and all blocks of newly grown ice are identified by using the region growing techniques, and get a 100 km maximum edge change per day threshold, for eliminating over-growth ice that is misclassified as ice in the ocean. An example of the final sea ice extent is shown in Fig. 4c.

4 Results

The algorithm described in the above section is used to generate polar sea ice extent maps of the Arctic and Antarctic regions for each day of 2013–2014 from HY-2A-SCAT backscatter data. A time series of ice mapped imagery can be used in the removal of sea ice regions in scatterometer wind processing and ice edge evolution studies. In this section, the ice extent maps are compared to the SIC products and SAR imagery.

4.1 *Sea ice mapping*

As mentioned previously, the FLDA algorithm is imported to produce operational polar daily ice extent imagery in the HY-2A satellite mission, which is classified by a dynamic threshold based on predicated ice extent in winter (i.e., from this year's October to next year's June). Figure 5 shows the seasonal and geographical sea ice products derived from HY2A-SCAT for a limited subset of days. For Arctic sea ice imagery, the image sequence of the largest stage, retreat, trough period and growth is separated for exhibition. In addition, Antarctic images of low ebb, expansion, largest stage and melt parse similarly demonstrate the seasonal variation of the ice pack.

4.2 *Comparison with SSMIS SIC*

We compared the ice extent results of the proposed method with SIC operational products of SSMIS. The two products have the same projection and spatial resolution. The total sea ice extent area is used as a parameter. This parameter of HY-2A-SCAT is calculated by summing the areas of all ice-masked pixels in its product. In order to compare datasets, SIC of SSMIS have thresholds at various concentration levels (0%, 15% and 30%) to obtain multiple ice edges. The total ice areas results for 2013 and 2014 of different products are shown in Fig. 6a for the Arctic and Fig. 6b for the Antarctic. The results show that the seasonal change of HY-2A-SCAT is similar with that of SSMIS. For the Arctic, the HY-2A-SCAT extent correlates very well with SSMIS 0% extent during ice decay and with 15% in other conditions. For the Antarctic, results also show a good agreement with SSMIS 15% extent for the whole period. The agreement with SSMIS 15% extent proves that HY-2A-SCAT detect the ice edge effectively because that 15% concentration contour from passive microwave fields corresponds most closely with the average true ice edge (Comiso and Zwally, 1984).

In order to illustrate the comparisons, a σ_H image over the Svalbard Islands (Fig. 7a) and Beaufort Sea (Fig. 7b) of October 13, 2013 is shown in Fig. 7. HY-2A-SCAT ice extent and 15% contour of SSMIS' SIC are overlapped with red and blue, respectively. In Fig. 7, the HY-2A-SCAT's result matches the SSMIS' 15% contour very well. However, over some parts (marked with red block) of Fig. 7b, the result of HY-2A-SCAT underestimates the sea ice extent and the 15% contour overlaps the ice edge of the σ_H image. The detailed difference analysis of sea ice edge detection with active scatterometer versus passive microwave radiometer is out of the range of this work and remains a challenge for further research (Remund and Long, 1999; Meier and Stroeve, 2008).

4.2 *Comparison with SAR*

The ice extent maps are compared with SAR imagery for qualitative visual comparison. For this study, several Sentinel-1 images were downloaded from the Polar View's website and overlapped with ice extent maps in ArcGIS. Because the Polar View supplies SAR images of the past 30 days, it is difficult to find SAR images of 2013 for visual comparison. Some sample SAR images of 2015 are shown in Fig. 8. Figures 8a and b show a winter SAR mosaic over Greenland Sea for October 23, 2015 and November 4, 2015. The HY-2A-SCAT ice extent shows good correlation with the SAR ice edge. During the winter, ice growth is expected and

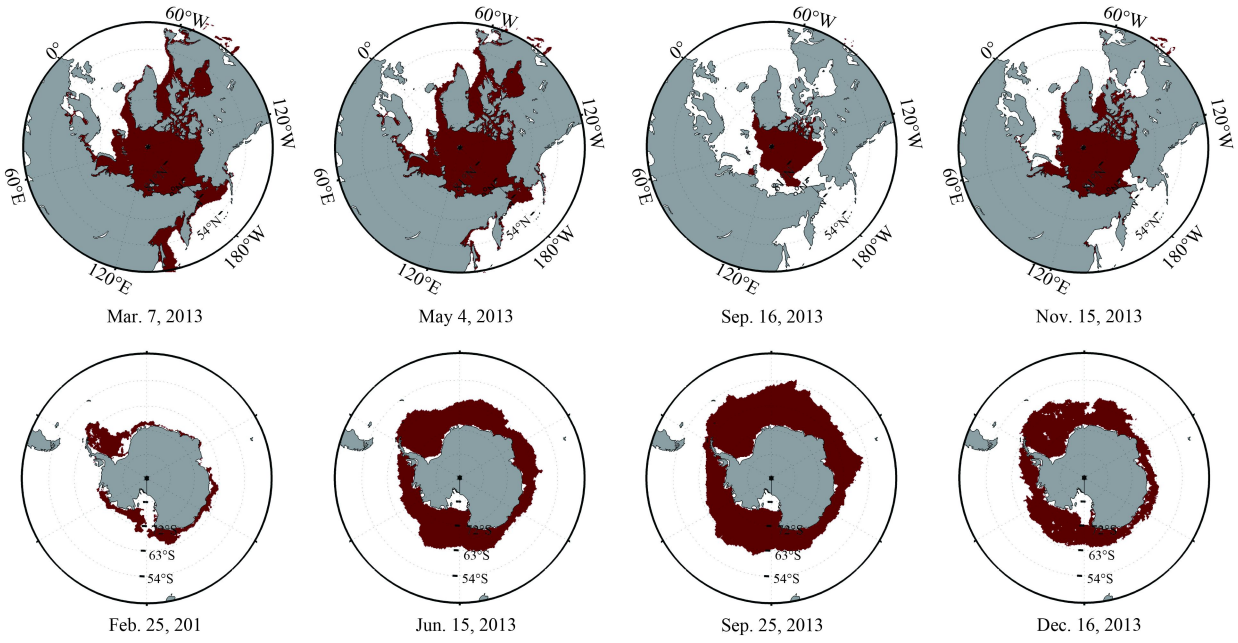

Fig. 5. Daily polar sea ice extent and Arctic sea ice type from HY-2A-SCAT (except September 16, 2013, because it is beyond the scope of ice type determination).

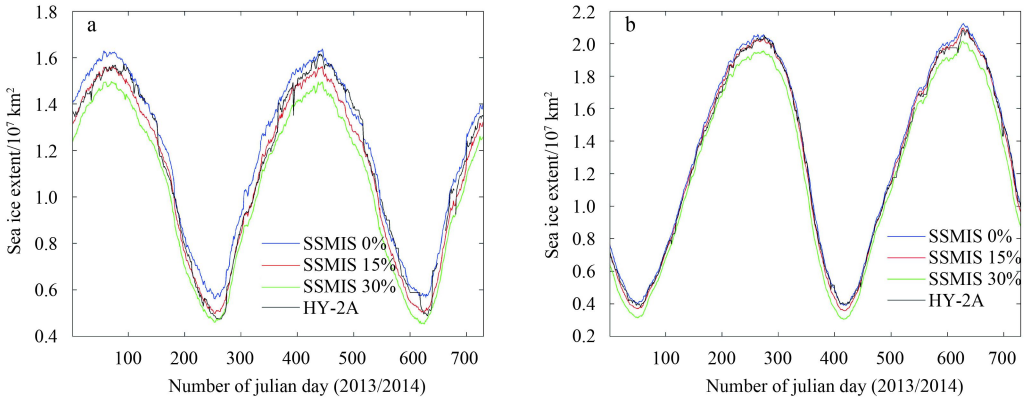

Fig. 6. Arctic (a) and Antarctic (b) daily total sea ice area of 2013–2014. The HY-2A-SCAT and SSMIS 0%, 15%, and 30% ice extents are shown for comparison.

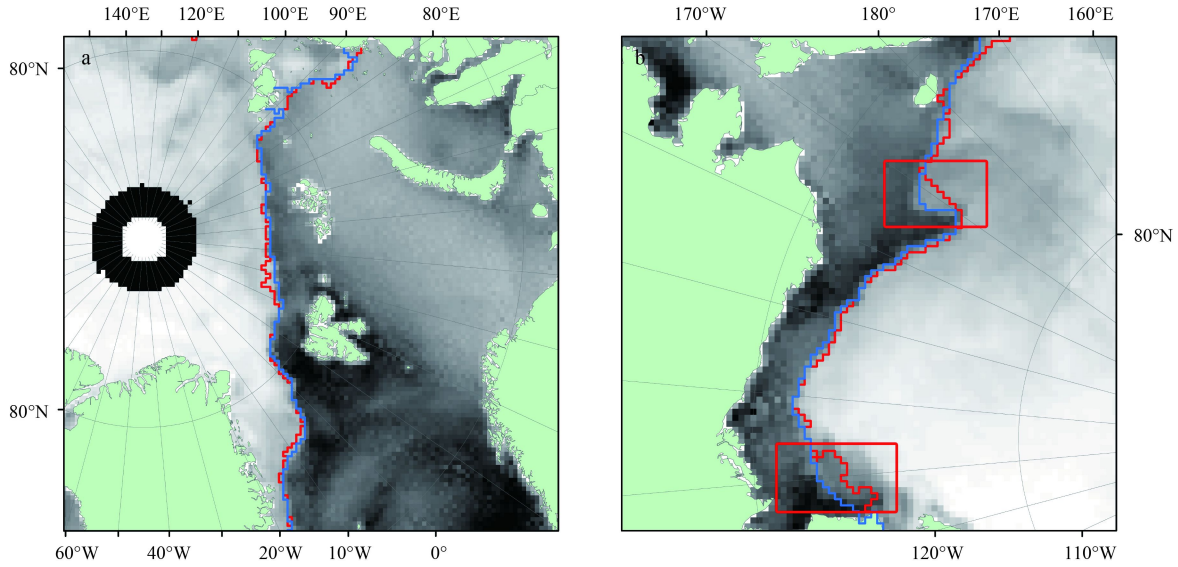

Fig. 7. Sea ice edge comparisons over the Svalbard Islands (a) and the Beaufort Sea on October 13, 2013. The background is the σ_H image of HY-2A-SCAT. The SSMIS 15% contour and HY-2A-SCAT ice edge is plotted in blue and red, respectively.

some area is covered by new ice (red block), which is not detected by HY-2A-SCAT. Off-ice winds happened with the above new ice formation. The ice was blown southward and new ice was formed by cold northerly winds over the area of the red block. The HY-2A-SCAT ice edge underestimates the ice extent in Fig. 8a, which should correspond to the movement of ice edge on October 23, 2015. Therefore, a comparison of the HY-2A-SCAT result with SAR is not straight forward, but it is another way to get the temporal variability of the ice edge.

Figures 8c and d show summer SAR images over Antarctic on October 20, 2015 and September 28, 2015. In Fig. 8c, the good correlation between the HY-2A-SCAT extent and SAR ice edge may be due to an obvious difference between ice and water and low wind speed over local area. Over the red block of Fig. 8d, the differences are very evident because sea ice edges can be very dynamic and move several kilometers in a single day. The HY-2A-SCAT edges represent averages over the entire day and the SAR imagery is a “snap-shot” of the ice edge at a particular time of day.

5 Conclusions

This paper established an algorithm to map the sea ice extent over the polar area based on the scatterometer data of HY-2A. The method is used to generate polar sea ice extent maps of the Arctic and Antarctic regions for each day of 2013–2014 from HY-2A-SCAT backscatter data. The retrieved ice extent maps are assessed with the operational SIC products of SSMIS and SAR imagery. The main conclusion of this research can be stated as follows:

(1) Four parameters are used for distinguishing between sea ice and ocean: mean HH backscatter (σ_H), backscatter polarization Ratio (σ_V /σ_H), daily standard deviation per pixel for HH ($\Delta\sigma_H$), and daily standard deviation per pixel for VV ($\Delta\sigma_V$). Through FLDA, these parameters are proven effective in identifying sea ice versus water. The image erosion and dilation technique is used to eliminate misclassified ice of open water.

(2) The time series of ice mapped imagery shows ice edge evolution and has a similar seasonal change trend with total ice area from SSMIS SIC data. For both hemispheres, the HY-2A-SCAT extent correlates very well with the SSMIS 15% extent.

(3) The ice extent maps are compared with SAR imagery for qualitative visual comparison. The HY-2A-SCAT ice extent shows good correlation with the Sentinel-1 SAR ice edge. The HY-2A-

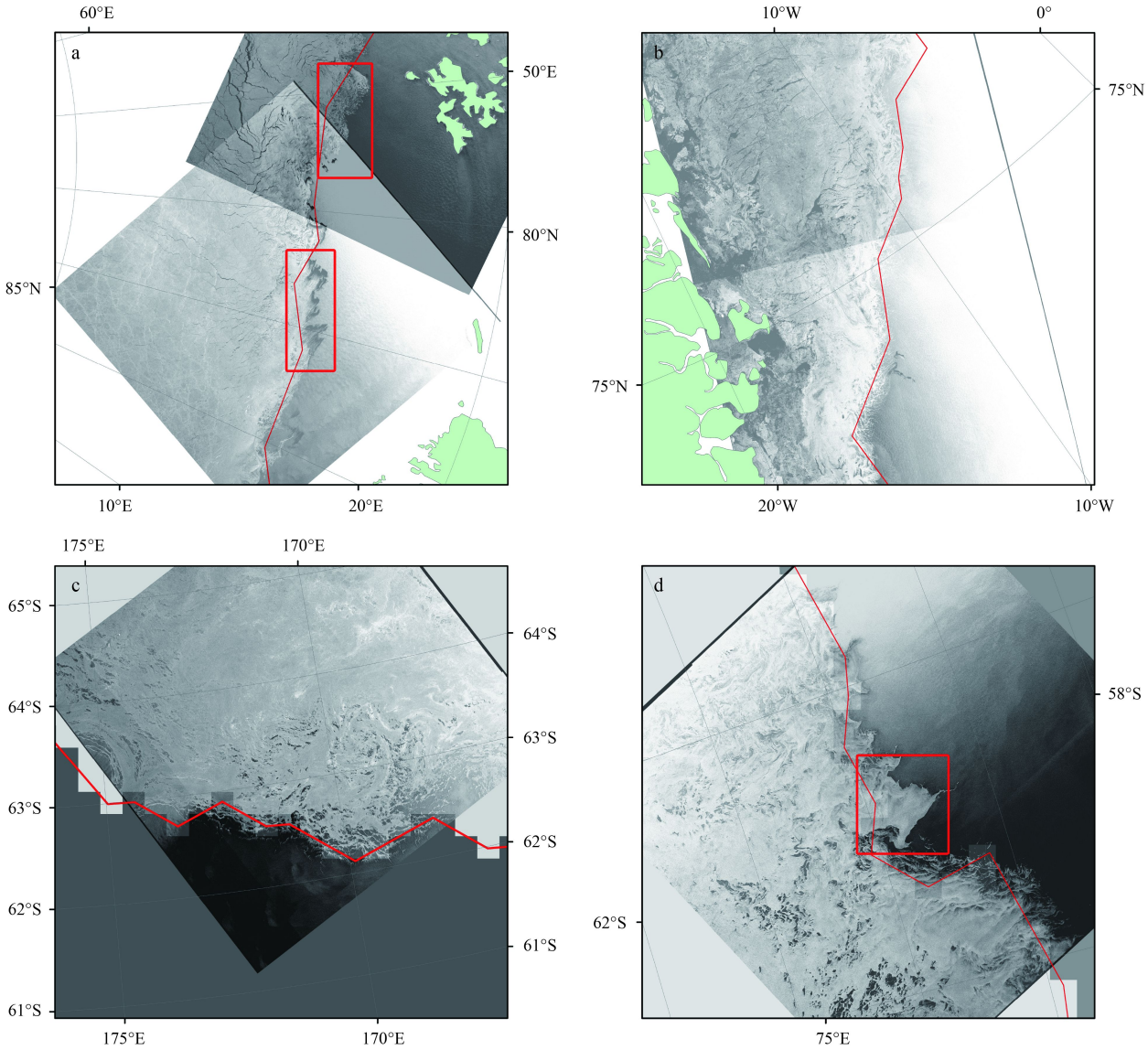

Fig. 8. Sentinel-1 imagery with HY-2A-SCAT ice extent. The image acquisition days are October 23 (a), November 4 (b), October 20 (c), and September 28 (d) of 2015.

SCAT edges represent averages over the entire day and the SAR imagery is a "snap-shot" of the ice edge at a particular time of day. So over some ice edge area with high wind speed, the difference is very evident because sea ice edges can be very dynamic and move several kilometers in a single day.

Acknowledgements

The authors thank the NSIDC for supplying the SIC data and the Polar View for supplying the SAR images.

References

Breivik L A, Eastwood S, Lavergne T. 2012. Use of c-band scatterometer for sea ice edge identification. IEEE Trans Geosci Remote Sens, 50(7): 2669–2677

Cavalieri D J, Parkinson C, Gloersen P, et al. 1996. Sea ice concentrations from Nimbus-7 SMMR and DMSP SSM/I-SSMIS passive microwave data, version 1. Boulder, Colorado USA: NASA National Snow and Ice Data Center Distributed Active Archive Center. http://dx.doi.org/10.5067/8GQ8LZQVL0VL [2014-1-31/2015-4-1]

Comiso J C, Zwally H J. 1984. Concentration gradients and growth/decay characteristics of the seasonal sea ice cover. J Geophys Res, 89(C5): 8081–8103

De Abreu R, Wilson K, Arkett M, et al. 2002. Evaluating the use of QuikSCAT data for operational sea ice monitoring. In: 2002 IEEE International Geoscience and Remote Sensing Symposium. Toronto, Ontario, Canada: IEEE, 5: 3032–3033

De Haan S, Stoffelen A. 2001. Ice discrimination using ERS scatterometer document external project: 2001, SAF/OSI/KNMI/TEC/TN/120, EUMETSAT. http://www.knmi.nl/publications/ [2001-12-31/2012-5-6]

Early D S, Long D G. 1997. Azimuthal modulation of c-band scatterometer σ^0 over southern ocean sea ice. IEEE Trans Geosci Remote Sens, 35(5): 1201–1209

Long D G, Drinkwater M R. 1994. Greenland ice-sheet surface properties observed by the seasat-a scatterometer at enhanced resolution. J Glaciol, 40(135): 213–230

Meier W N, Stroeve J. 2008. Comparison of sea-ice extent and ice-edge location estimates from passive microwave and enhanced-resolution scatterometer data. Ann Glaciol, 48(1): 65–70

Remund Q P, Early D S, Long D G. 1997. Azimuthal Modulation of Ku-band Scatterometer Sigma-0 over the Antarctic. Provo, UT, USA: MERS

Remund Q P, Long D G. 1997. Automated Antarctic ice edge detection using NSCAT data. In: 1997 IEEE International Remote Sensing—A Scientific Vision for Sustainable Development, Geoscience and Remote Sensing. Singapore: IEEE, 4: 1841–1843

Remund Q P, Long D G. 1999. Sea ice extent mapping using Ku band scatterometer data. J Geophys Res, 104(C5): 11515–11527

Remund Q P, Long D G. 2014. A decade of quikSCAT scatterometer sea ice extent data. IEEE Trans Geosci Remote Sens, 52(7): 4281–4290

Remund Q P, Long D G, Drinkwater M R. 2000. An iterative approach to multisensor sea ice classification. IEEE Trans Geosci Remote Sens, 38(4): 1843–1856

Rivas M B, Stoffelen A. 2011. New bayesian algorithm for sea ice detection with quikSCAT. IEEE Trans Geosci Remote Sens, 49(6): 1894–1901

Tonboe R, Toudal L. 2005. Classification of new-ice in the Greenland sea using satellite SSM/I radiometer and SeaWinds scatterometer data and comparison with ice model. Remote Sens Environ, 97(3): 277–287

Yueh S H, Kwok R, Lou S H, et al. 1997. Sea ice identification using dual-polarized ku-band scatterometer data. IEEE Trans Geosci Remote Sens, 35(3): 560–569